Pulsed-power plasma reactors: two-dimensional electropositive discharge simulation in a GEC reference cell

Badri Ramamurthi[1] **and Demetre J Economou**[1,2]

[1] Plasma Processing Laboratory, Department of Chemical Engineering, University of Houston, Houston, TX 77204-4004, USA

E-mail: economou@uh.edu

Abstract

A two-dimensional self-consistent continuum model was developed to study the spatio-temporal dynamics of a pulsed power (square-wave-modulated) inductively coupled electropositive (argon) discharge. The coupled equations for plasma power deposition, electron temperature and charged and neutral species densities were solved to obtain the space–time evolution of the discharge in a gaseous electronics conference (GEC)-ICP reference cell. The Ar* metastable density was governed by gas phase reactions since the diffusion time was longer than the pulse period. This resulted in complex Ar* density profiles as a function of time during a pulse. The time-average ion flux to the substrate in the pulsed plasma reactor was larger than that in a continuous wave reactor, for the same energy input. The effect of control parameters such as power, duty ratio, pressure and pulse frequency on the evolution of electron density was investigated. Simulation results on electron density and temperature were in reasonable agreement with available experimental data.

1. Introduction

Low-pressure (<100 mTorr) glow discharge plasmas are used extensively in microelectronics processing for etching and deposition of thin films [1]. Pulsed power operation (e.g. square-wave-modulated power input to the plasma) may offer potential improvements of reactor performance, compared to continuous wave (CW) plasma reactors. For example, etch or deposition rate and uniformity may be improved [2, 3], particulate density may be reduced [4], or anomalous etch profiles may be suppressed [5, 6].

In order to improve understanding of pulsed plasmas, and elucidate how these plasmas may affect processing, it is worthwhile to model the spatio-temporal plasma evolution in realistic reactor geometries. Existing pulsed plasma reactor models and simulations are limited to well-mixed (0-D) [7–9] and one-dimensional (1-D) works [10, 11]. In this paper, we demonstrate a two-dimensional (2-D) self-consistent fluid simulation to study the spatio-temporal evolution of

an inductively coupled pulsed argon discharge in a gaseous electronics conference (GEC) reference cell [12]. In previous studies, a modular approach was used to simulate CW plasma operation, in which only the 'steady state' was of interest [13]. In contrast, in this work, the coupled equations for plasma power deposition, electron temperature, and charged and neutral species densities were solved simultaneously to capture the time-dependent discharge evolution. To our knowledge, there has been no published report on the self-consistent 2-D simulation of pulsed plasmas so far.

2. Model formulation

Figure 1 shows a schematic of an inductively coupled GEC reference cell, which can generate a high-density plasma inside a chamber bounded by a quartz window and metal walls. The plasma is driven by a 5-turn planar coil powered at 13.56 MHz. The RF current in the coil produces a time-varying magnetic field, which in turn induces an azimuthal electric field heating the plasma electrons. The model consists of an electromagnetic equation for the self-consistent

---

[2] Author to whom correspondence should be addressed.

azimuthal electric field powering the plasma, an equation for the electron temperature (assuming Maxwellian electrons), and mass continuity equations for the charged (Ar$^+$) and neutral (metastables, Ar*) species. The model equations are described in the following sections. Details of the formulation may be found in published works [14, 15]. The electron density is calculated by charge neutrality (in this case it is identical to the ion density). This implies that the thin sheath near the reactor walls is not included in the simulation. Since the sheath is only 100 s of microns thick in the high-density plasma, boundary conditions are effectively applied at the geometric location of the walls. The reaction set for argon (table 1) was the same as before [16].

The assumptions of the model were as follows:

(a) the fluid approximation was used since $\lambda/L = 0.1$, where λ is mean free path of the species ($\sim$0.5 cm) and L is a characteristic dimension of the reactor ($\sim$5 cm);

(b) the densities, electron temperature and induced electric field of the species were assumed to be azimuthally symmetric (2-D, r–z system);

(c) the charged particle flux was described by the drift-diffusion approximation (spatial inertia was neglected in the momentum equations), since the pressure was >10 mTorr;

(d) the electron energy distribution function (EEDF) was assumed Maxwellian and an equation for the electron temperature was solved;
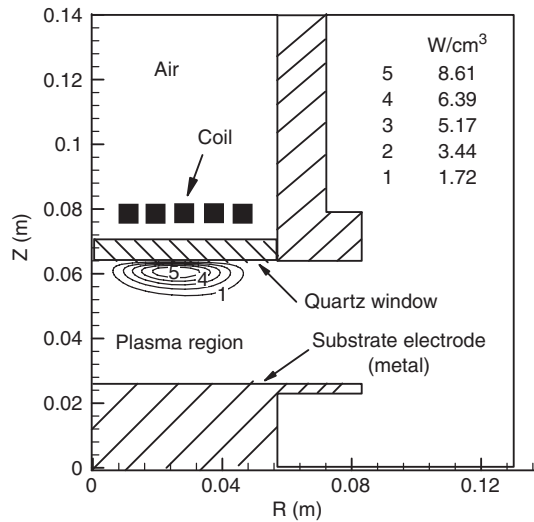

Figure 1. Schematic of the GEC-ICP reactor used in the simulation. The power deposition profile 50 μs into the pulse is also shown (for base case parameter values shown in table 2).

Table 1. Reaction set used in the simulation.

No	Process	Reaction	H_j (eV)
R1	Ground-state excitation	Ar + e → Ar* + e	11.6
R2	Ground-state ionization	Ar + e → Ar$^+$ + 2e	15.7
R3	Stepwise ionization	Ar* + e → Ar$^+$ + 2e	4.1
R4	Superelastic collisions	Ar* + e → Ar + e	−11.6
R5	Metastable quenching	Ar* + e → Ar^r + e	0.1
R6	Metastable pooling	Ar* + Ar* → Ar$^+$ + Ar + e	
R7	Two-body quenching	Ar* + Ar → 2Ar	
R8	Three-body quenching	Ar* + 2Ar → Ar$_2$ + Ar	

(e) particle mobilities and diffusivities were assumed constant for a given pressure;

(f) electron heating was assumed to be collisional (Ohmic). Non-collisional heating can become important when the effective electron mean free path exceeds the skin depth [17];

(g) ions and neutrals were assumed to be at a constant temperature. Hence, a heavy species energy equation was not solved.

2.1. Electromagnetics

Under the assumption of azimuthally symmetric electric field, Maxwell's equations can be reduced to a single scalar equation in E_θ:

$$\frac{1}{r}\frac{\partial}{\partial r}\left(r\frac{\partial E_\theta}{\partial r}\right) + \frac{\partial^2 E_\theta}{\partial z^2} - \frac{E_\theta}{r^2} + \frac{\omega^2}{c^2}K_c E_\theta = -j\omega\mu_0 J_\theta, \quad (1)$$

where ω is the driving frequency of the coil current, μ_0 is the vacuum permeability, K_c is the complex permittivity of the plasma (which depends on the electron density), J_θ is the impressed current density in the coils and c is the speed of light. At low frequencies, the current in the coil is nearly constant and the above equation may be solved to determine E_θ in the reactor. However, at higher frequencies, a circuit model is required to account for capacitive coupling between the coil and the plasma (the current changes from loop to loop) [18, 19]. The power deposited in the plasma was computed by

$$P = \tfrac{1}{2}\mathrm{Re}\,(\sigma_p)|E_\theta|^2, \quad (2)$$

where $\mathrm{Re}\,(\sigma_p)$ is the real part of σ_p, the complex plasma conductivity. Equation (2) assumes that the power deposited in the plasma is due to Ohmic heating. The conductivity was obtained from the following relations:

$$K_c = 1 - \frac{\omega_{pe}^2}{\omega^2(1 + j\nu_m/\omega)}, \quad (3)$$

$$\sigma_p = -j\omega\varepsilon_0(K_c - 1), \quad (4)$$

where

$$\omega_{pe}^2 = \frac{n_e e^2}{m\varepsilon_0} \quad (5)$$

is the electron plasma frequency and ν_m is the electron momentum–exchange collision frequency.

The right-hand side of equation (1) includes only the current in the coil, J_θ. The (induced) current in the plasma is accounted for by the term involving the plasma permittivity, K_c, on the left-hand side of equation (1).

2.2. Ion transport and reaction

With the drift-diffusion flux approximation for the charged species, the continuity equation for positive ions (Ar$^+$) is of the form

$$\frac{\partial n_i}{\partial t} = -\nabla\cdot(z_i\mu_i n_i \vec{E}_{sc} - D_i\nabla n_i) + \sum_j R_{ji}, \quad (6)$$

where n_i, z_i, D_i and μ_i are the positive ion density, charge number, diffusivity, and mobility, respectively. $\vec{E}_{sc}$ is the electrostatic (space charge) field having two components (E_r and E_z). The summation on the right-hand side represents

325

gas-phase reactions that produce (reactions R2, R3, and R6 of table 1) or destroy (none here) ions. Boundary conditions were $\vec{\Gamma}_i = 0$ on the symmetry axis/plane ($\vec{\Gamma}_i$ is the ion flux), and $n_i \approx 0$ on the walls. Ions are thus lost by ambipolar diffusion to the walls. The electrostatic field was derived assuming no net current in the plasma:

$$\vec{E}_{sc} = \frac{D_i \nabla n_i - D_e \nabla n_e}{\mu_i n_i + \mu_e n_e}. \tag{7}$$

The electron density n_e was obtained from quasi-neutrality as $n_e = n_i$.

2.3. Electron temperature

The electron energy equation reads as

$$\frac{\partial}{\partial t}\left(\frac{3}{2}n_e T_e\right) = -\nabla \cdot \vec{q}_e + P - \sum_j R_{je} \Delta H_j, \tag{8}$$

$$\vec{q}_e = -K_e \nabla T_e + \tfrac{5}{2}\vec{\Gamma}_e T_e, \tag{9}$$

where $\vec{q}_e$ is the electron energy flux, K_e is the electron thermal conductivity and $\vec{\Gamma}_e$ is the electron flux. The second term on the right-hand side of (8) represents the power deposited into the electrons (equation (2)). The third term on the right-hand side of (8) represents the electron energy lost due to elastic and inelastic collisions. The boundary conditions were: $\vec{q}_e = 0$ on the symmetry axis/plane and $\vec{q}_e = \frac{5}{2}\vec{\Gamma}_e T_e$ along material boundaries. Since the timescale for electron temperature evolution is the smallest in the system ($\sim 0.1\,\mu$s), the temperature reaches a periodic steady state most rapidly.

2.4. Metastable transport and reaction

The Ar* metastable density was computed using equation (10) below assuming that transport is diffusion dominated:

$$\frac{\partial n_*}{\partial t} = -\nabla \cdot (-D_* \nabla n_*) + \sum_j R_{j*} - \frac{n_*}{\tau_{res}}, \tag{10}$$

where R_{j*} represents reactions that produce or consume Ar*. A 'composite' state was used to represent the long lived metastables ($^3P_0$ and $^3P_2$ levels). Metastable reactions included production by excitation of ground state Ar (reaction R1 of table 1), and destruction by reactions R3–R8 of table 1. Three-body reactions (R8) were negligible under the low operating pressure. The last term in equation (10) accounts for convective flow losses of Ar* atoms through the residence time τ_{res} ($= 3.8$ ms). Flow losses turn out to be negligible. The boundary conditions were zero gradient of density along the symmetry axis/plane ($\partial n_*/\partial r = 0$, $\partial n_*/\partial z = 0$), and $-D_* \nabla n_* = (\gamma/2(2 - \gamma))n_* v_*$ on walls, according to the Chantry [20] boundary condition. Here D_* is the diffusivity of Ar* in Ar, γ is the destruction probability of Ar* atoms on walls (taken as unity) and v_* is their thermal velocity. The total gas density was found assuming a uniform pressure and a gas temperature of 300 K. The response timescale of metastables is the largest in the system (~ 1 ms). Therefore, integration in time had to be performed over 10–100 s of pulse periods to attain a periodic steady state.

Gas heating was not accounted for in this work. Gas heating will result in lower gas number density (for a constant pressure). To a first approximation, the effect of gas heating may be ascertained by looking at the effect of pressure. For a given (constant) gas temperature, as assumed in this work, a lower pressure will lead to lower gas density.

3. Method of solution

The set of nonlinear coupled partial differential equations for T_e and species transport (equations (6), (8) and (10)) was spatially discretized using a streamline upwind Petrov–Galerkin (SUPG) method [21] to yield a system of equations of the form

$$A(u)\dot{u} = K(u)u + F(u), \tag{11}$$

where u represents the solution vector, $\dot{u}$ is the time derivative of u, and A and K are banded nonlinear mass and stiffness matrices, respectively. F is a nonlinear source vector. The resulting set of implicit ordinary differential equations in equation (11) was integrated in time using backward difference formulae [22] until a periodic steady state was obtained. At each time step, the equation for the azimuthal electric field (equation (1)) was solved using the Galerkin finite element method and a direct band solver. The convergence criterion was set by evaluating the L^2 norm of the solution normalized with respect to the average i.e.

$$\varepsilon_j = \frac{1}{V^{1/2}}\left[\int_\Omega \left\{\left(\frac{u_j}{\langle u_j\rangle}\right)_{(i+1)T_p} - \left(\frac{u_j}{\langle u_j\rangle}\right)_{iT_p}\right\}^2 d\Omega\right]^{1/2}, \tag{12}$$

where, for each variable j, ε_j, u_j and $\langle u_j\rangle$ are a tolerance parameter, value of that variable (e.g. ion density) and its average, respectively, over the domain of interest Ω. V is the plasma volume, T_p is the pulse width of the power modulation cycle and i is the cycle number ($i = 1, 2, 3, \ldots$). The convergence criterion was tested at the end of each cycle. Integration was terminated when the evaluated tolerance was less than a user-specified value (0.5%) for all species and electron temperature. As expected, the Ar* atom density was the slowest to converge.

4. Results and discussion

An argon discharge was simulated in an inductively coupled GEC reference cell under the base case parameters shown in table 2. The ion mobility and metastable diffusivity are shown in table 3 [16]. The ionic diffusivity was computed using the Einstein relation $D = \mu kT/e$, where T is temperature. Power to the plasma was square-wave-modulated with the power at the peak value for the first $50\,\mu$s of the pulse (power on) followed by zero power (power off) for the remaining $50\,\mu$s

Table 2. Base case operating parameters.

Pressure	20 mTorr
Peak power	300 W
Pulse frequency	10 kHz
Duty ratio	0.5
Ar* wall 'deactivation' probability	1
Ion temperature	0.026 eV
Gas temperature	300 K

(pulse period $100\,\mu s$, duty ratio of 0.5). The 'power on' and 'power off' phases of the cycle will be referred to as 'active glow' and 'afterglow', respectively. Besides the base case run, simulations were also performed for duty ratios of 0.3, 0.5 and 0.7, peak powers of 290, 190 and 165 W, and pulse frequencies of 20, 10 and 5 kHz in order to study their effect on electron density and compare simulation results with experiments [23]. All results shown below are for the *periodic steady state* at the base case parameters, unless noted otherwise. In the discussion below, the discharge 'core' and 'periphery' refer to the core and periphery regions, respectively, of the space in between the parallel plates, while 'outer region' refers to the cylindrical space surrounding them (figure 1).

The quasi-steady-state power deposition profile (in $W\,cm^{-3}$) is also shown in figure 1. Power is deposited directly under the coil in a toroidal pattern, with a typical skin depth of $\sim 1\,cm$. The max power density is $\sim 9.5\,W\,cm^{-3}$ for a total power deposition of 300 W.

The evolution of ion (and electron) density, metastable density and electron temperature at the *centre* of the reactor ($R = 0$ and $z = 4.5\,cm$) is shown in figure 2. A spike in electron temperature is observed $\sim 1\,\mu s$ into the active glow as power is deposited into a relatively smaller number of electrons. The electron temperature quickly ($\sim 10\,\mu s$) reaches a quasi-steady value later in the active glow, only to drop precipitously in the early afterglow, due to inelastic collision losses with Ar and Ar* atoms. The temperature decay rate in the late afterglow is much smaller because inelastic collisions (large energy sink) are quenched. Also, superelastic collisions (reaction R4 in table 1) provide some energy back to the electron gas. All features of the temperature evolution seen here have also been observed experimentally [6, 23]. The ion

Table 3. Species mobility and diffusivity (from [16]).

Name	Symbol	Value
Ar$^+$ mobility	$N\mu_+$ (cm^{-1} V^{-1} s^{-1})	4.65×10^{19}
Ar* diffusivity	ND_* (cm^{-1} s^{-1})	2.42×10^{18}

(electron) density increases in the active glow due to ionization (reactions R2 and R3 in table 1), reaching a plateau also at $\sim 10\,\mu s$ into the active glow. The decay rate of ions in the afterglow is characterized by the ambipolar diffusion time constant (τ_d), since the ion density is high enough (Debye length $\ll$ reactor length) even at the end of the pulse for a plasma to exist throughout the pulse. The estimated decay time constant of $\tau_d = (L/\pi)^2/D_a \sim 10\,\mu s$ agrees with that extracted from figure 2. In contrast, metastables are quickly lost at the centre of the reactor (see also figure 5) mainly due to quenching by electrons to the resonant state (reaction R5).

Figure 3 shows the quasi-steady electron temperature profile, $20\,\mu s$ in the active glow. The electron temperature is highest ($\sim 3.7\,eV$) where the power deposition is maximum (see figure 1). Despite the fact that power is deposited in a small toroidal zone under the coil, electrons are substantially warm near the substrate and in the outer region of the reactor ($8 < R < 13\,cm$) due to the high thermal conductivity of the electron gas (remember that electron thermal conductivity is proportional to the electron density). Lower pressures would lead to higher electron temperatures and more uniform temperature distributions.

The evolution of Ar$^+$ density is shown in figure 4 at times of 0.5, 5, 50, 60, 70 and $90\,\mu s$ during a pulse. Ions are confined between the parallel plates with a significant gradient in the radial direction. This results in highly non-uniform flux of ions bombarding the substrate electrode (see also figures 6 and 7). The ion density increases by two orders of magnitude during the active glow (figures 4(a)–(c)). The ion density is asymmetric with respect to a horizontal plane through the centre of the discharge during the active glow due to the asymmetry in power deposition. The ionization rate is highest under the coils, yet diffusion helps to 'fill in' the discharge core, especially in the late active glow (figure 4(c)). Thus the ion density is maximum at $R = 0$. The ion density attains very high values ($\sim 10^{12}\,cm^{-3}$) late in the active glow due to the high power density. In the afterglow (power off), the ion density keeps decreasing (figures 4(d)–(f)) while
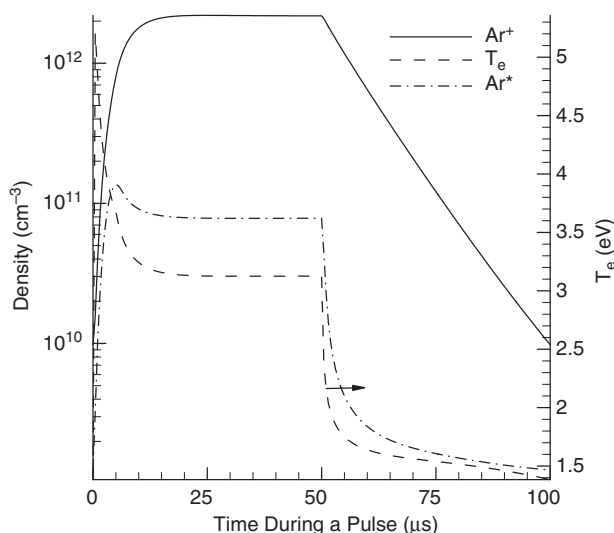

Figure 2. Argon ion (and electron), metastable density and electron temperature evolution at the discharge centre. Parameter values at base case are shown in table 2.
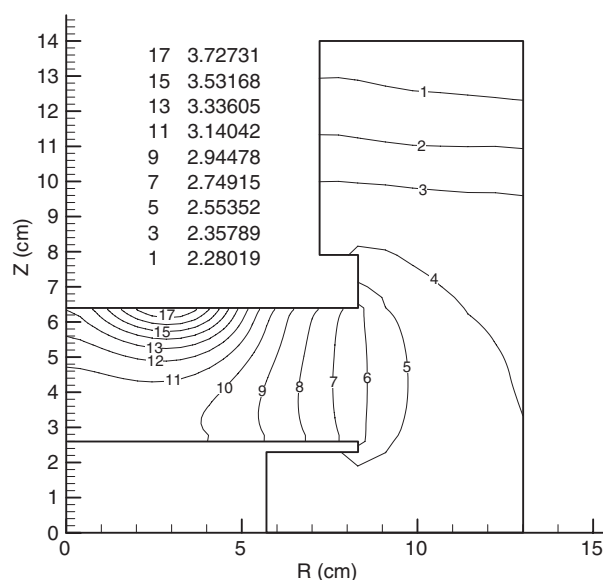

Figure 3. Electron temperature profile $20\,\mu s$ into the pulse. Parameter values at base case are shown in table 2.
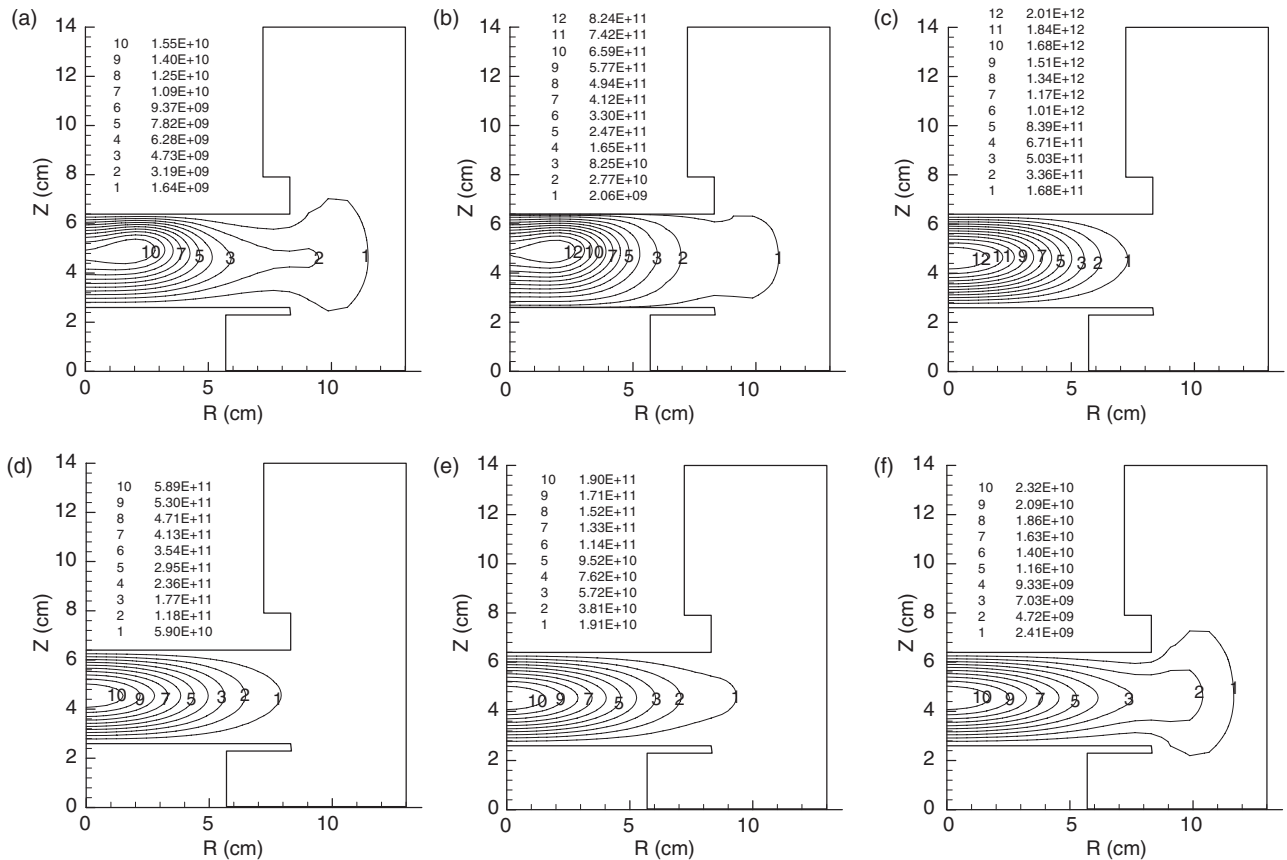
Figure 4. Ar⁺ (and electron) density evolution for times: (*a*) 0.5 μs, (*b*) 5 μs, (*c*) 50 μs, (*d*) 60 μs, (*e*) 70 μs and (*f*) 90 μs during a pulse. Parameter values at base case are shown in table 2. Note the different density scale for each frame.

the profile tends to be less asymmetric with respect to the horizontal plane through the centre of the discharge.

The metastable diffusion time is a few ms, much longer than the pulse period. Thus, the evolution of metastable density during a pulse, figure 5, is governed by volumetric reactions. Metastable quenching by electrons to resonant states (reaction R5 in table 1) has a time constant of several μs for an electron density of 5×10^{11} cm^{-3}. Very early in the active glow, figure 5(*a*), the Ar* density is larger in the outer region of the reactor due to destruction of metastables in the plasma during the afterglow of the previous pulse. The metastable density then rises forming a peak in the plasma core, as production of metastables by excitation (reaction R1) picks up (figure 5(*b*)). The timescale for electron temperature evolution is much smaller than that of metastable evolution. Consequently, excitation is the dominant reaction in the initial active glow leading to a sharp increase in metastable density. (The stepwise ionization loss rate is low, despite a smaller threshold, due to the low metastable density at the start of a pulse.) As the metastable density rises, so do destruction reactions, bringing about a quasi-steady-state of the metastable density (figure 5(*c*)). In the afterglow, figures 5(*d*)–(*f*), the production rate (by excitation) decreases sharply due to the large threshold (11.56 eV) and the fact that the electron temperature plummets (figure 2). This, coupled with loss reactions, leads to a dramatic decrease in metastable density in the discharge core. The main losses are due to quenching to resonant states (reaction R5) and stepwise ionization (which has a threshold of 4.14 eV) in the

early afterglow, and quenching to resonant states in the late afterglow. There is a faster depletion rate of metastables at the core, since electrons are much more abundant there. The results of figure 5 will not change appreciably if the metastable deactivation coefficient on the walls is taken to be less than unity, since the importance of volumetric reactions will then be even greater.

Since surface reaction (film etching or deposition) rates can strongly depend on the magnitude of the ion flux incident on the wafer, the Ar⁺ ion flux evolution was investigated. Figures 6 and 7 show the time-average (over a pulse period at the periodic steady state) radial profile of ion flux as a function of duty ratio and pressure, respectively. The ion flux profiles are very non-uniform reflecting the fact that the plasma is rather confined in the space between the parallel plates (figure 3). Increasing the duty ratio increases the time-average power deposition in the plasma (for the same peak power), consequently increasing the time-average ion flux, in a nearly linear fashion. The ion flux obtained in a CW reactor under the same conditions and with the same energy input (150 W CW vs 300 W of pulsed at 0.5 duty ratio) is lower than the pulsed reactor case. The trend is not quite so obvious when pressure is varied. In the pressure range investigated (10–40 mTorr), the peak ion density increased with pressure (not shown). However, as pressure increases, both the ion drift flux (which depends on electron temperature) and the ion diffusion flux decrease, leading to a drop of the total ion flux with pressure.
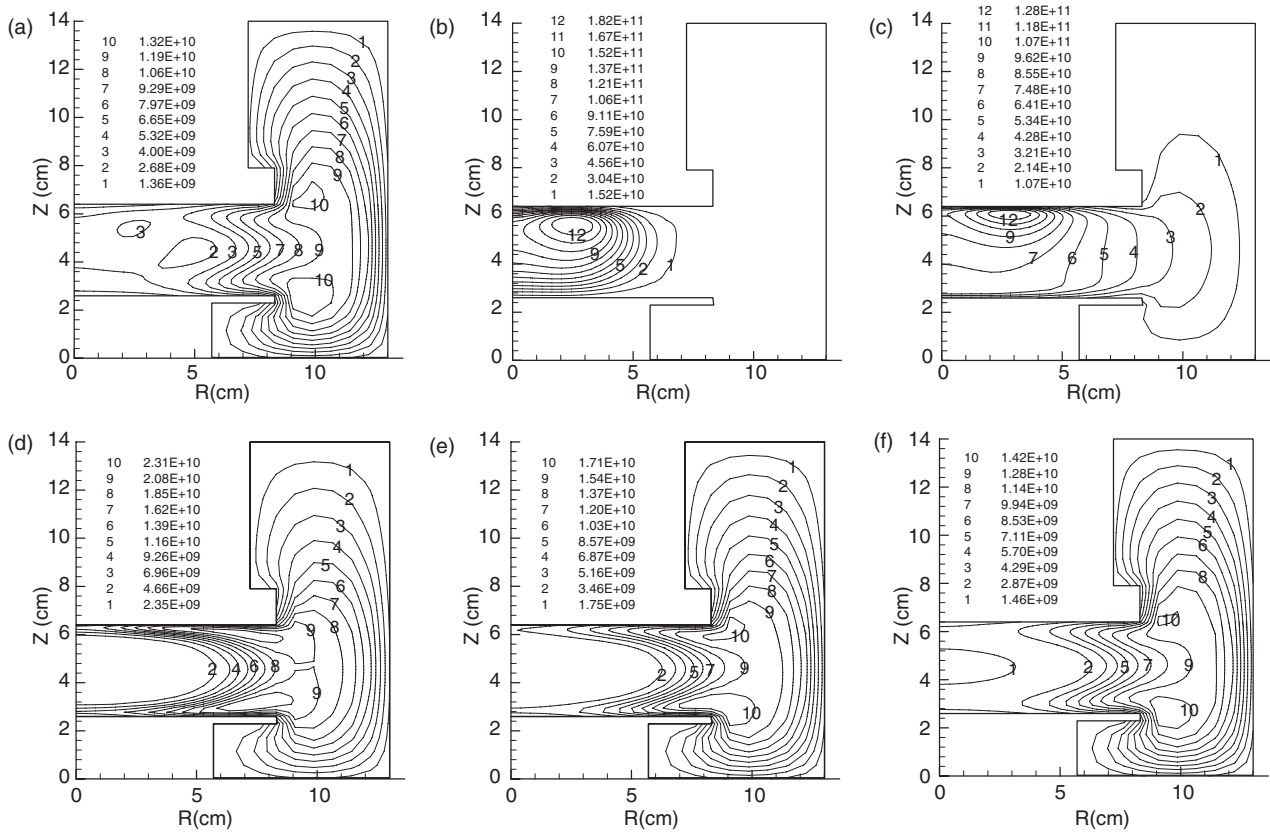
Figure 5. Ar* metastable density evolution for times: (*a*) 0.5 μs, (*b*) 5 μs, (*c*) 50 μs, (*d*) 60 μs (*e*) 70 μs and (*f*) 90 μs during a pulse. Parameter values at base case are shown in table 2. Note the different density scale for each frame.
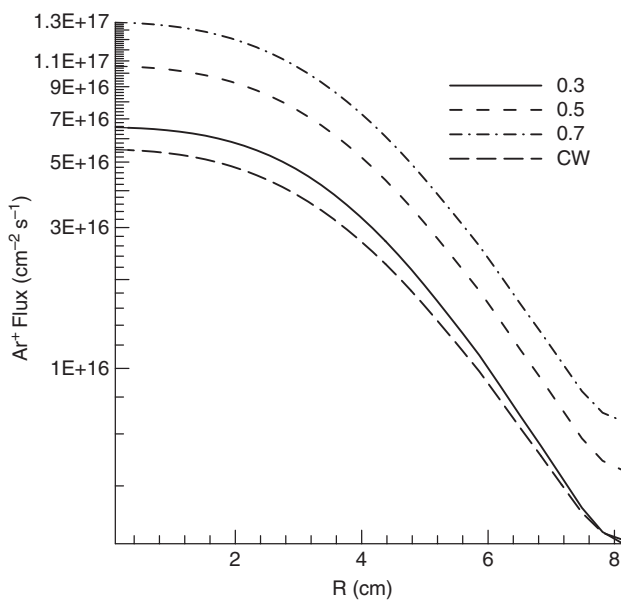

Figure 6. Effect of duty ratio on the time-average positive ion flux on the wafer. Ion flux for a CW plasma at the same energy input (150 W) is also shown. Other parameter values at base case are shown in table 2.

Figure 7. Effect of pressure on the time-average positive ion flux on the wafer. Other parameter values are shown in table 2.

4.1. Comparison with experimental data

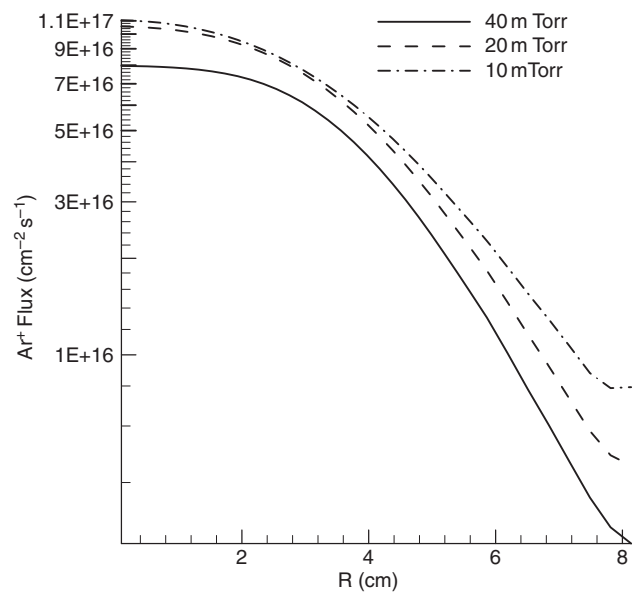The time evolution of electron density as duty ratio, peak power and pulse frequency are varied is shown in figure 8. The line-integrated densities are shown (obtained by integrating the electron density radially at the central plane $z = 4.5$ cm) to facilitate comparison with experimental data [23]. Figure 8(*a*) shows that the predicted electron density plateau is virtually unchanged as the duty ratio is varied. This implies that the plasma can reach a quasi-steady-state during
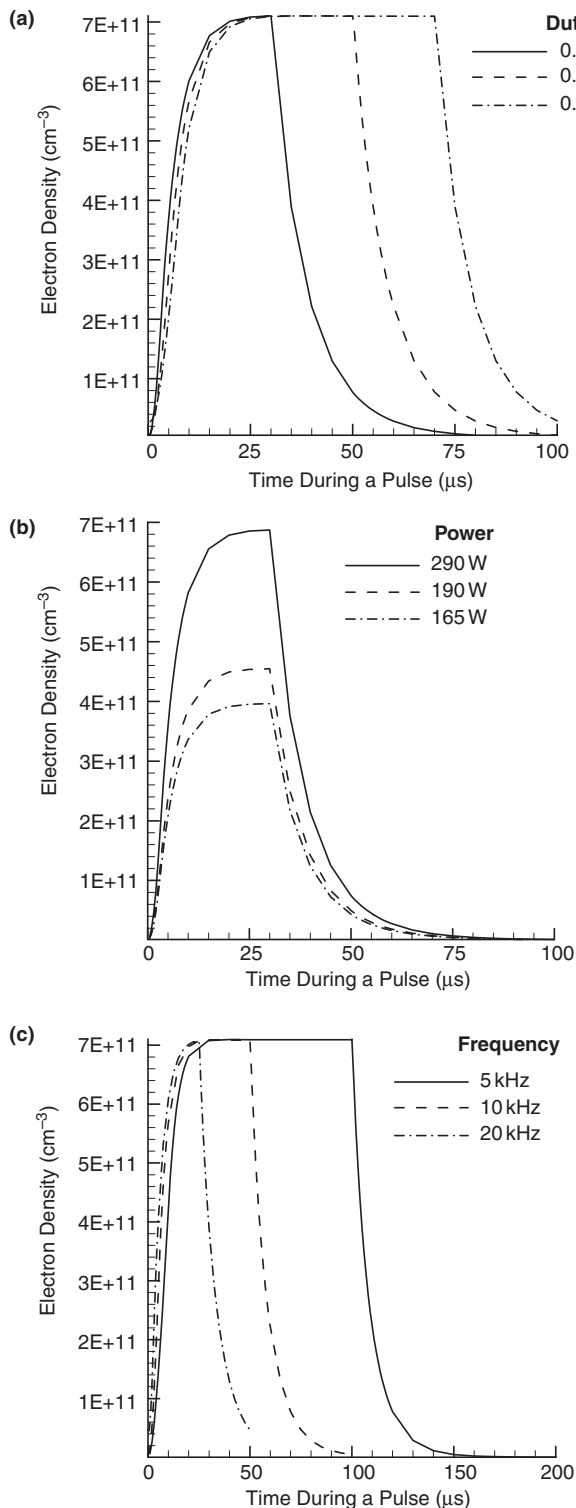
(a)

(b)

(c)

Figure 8. Effect of (*a*) duty ratio (*b*) peak power and (*c*) pulse frequency on line-integrated (along the central plane) electron density. Other parameter values are shown in table 2.

the active glow for all three duty ratios, i.e. the 'plasma on' fraction of the cycle (30, 50 and 70 μs for duty ratios of 0.3, 0.5 and 0.7, respectively) is 'long enough'. This is verified by looking at the electron density evolution of figure 2; n_e reaches a plateau after $\sim$10 μs in the pulse. Since the peak

power (300 W) was unchanged in figure 8(*a*), the peak electron density also remains the same. Of course, the time-average electron density increases in accord with the time-average power, as the duty ratio increases. Figure 8(*a*) also implies that metastables do not have much influence on electron density (except perhaps on the rising part of the n_e curves), since the metastable density did change as the duty ratio was varied from 0.3 to 0.7. Experimental data [23] show a different response: the electron density plateau initially increased with increasing duty ratio and then decreased with further increases in the duty ratio. The variations, however, were of the order of $\pm$10%, perhaps within the experimental uncertainty of the n_e measurement and/or the uncertainty of the measurement of the actual power dissipation in the plasma. The effect of power on electron density is shown in figure 8(*b*). The quasi-steady (plateau) value of electron density varies nearly linearly with power, in accord with experimental measurements. Finally, for a fixed duty ratio, the time-average power remains constant as the pulse period increases. Since the 'power on' fraction of the cycle is larger than the timescale of electron density evolution, the same quasi-steady value of electron density is attained as the pulse period is increased (figure 8(*c*)). Experiments also seem to support this trend [23].

Further comparisons between simulation and experiment were performed for CW discharges (no pulsing) also in the GEC-ICP reference cell. The steady-state electron density and electron temperature computed at the centre of the discharge ($R = 0$; $z = 4.5$ cm) are shown in figure 9 along with experimental data [24]. All trends are captured rather well. The electron density increases (nearly linearly) with power and the electron temperature remains virtually constant with power. The absolute electron densities are predicted reasonably well, but the simulation overpredicts the electron temperature, especially at low pressures. However, the simulation results for electron temperature are seen to be in much better agreement with a different set of data (taken from figure 11 of [12]) obtained for a pressure of 10 mTorr also in a GEC-ICP cell. The difference may lie in the fact that the two sets of data used a different probe (single probe vs double probe). Also, the grounded electrode was covered by a silicon wafer in [12]. Finally, figure 10 shows quite reasonable agreement of simulation predictions with experimental data (figure 11 of [12]) of *spatial profiles* of electron density and temperature. Comparisons are made at an axial position of 15 mm above the grounded (lower) electrode for 10 mTorr and 245 W.

5. Conclusions

A 2-D simulation of an inductively coupled, pulsed-power, electropositive discharge was developed based on the fluid approximation. An argon plasma sustained in a GEC reference cell, modified for inductive operation, was examined. An equation for the azimuthal electric field was solved to calculate the inductive power deposition. The latter was coupled self-consistently to the plasma transport equations, to capture the spatio-temporal evolution of the discharge during a pulse. The electron temperature was found to peak in the region of power deposition (under the coils). Considerably warm electrons persisted away from the power deposition zone due to the high thermal conductivity of the electron gas at
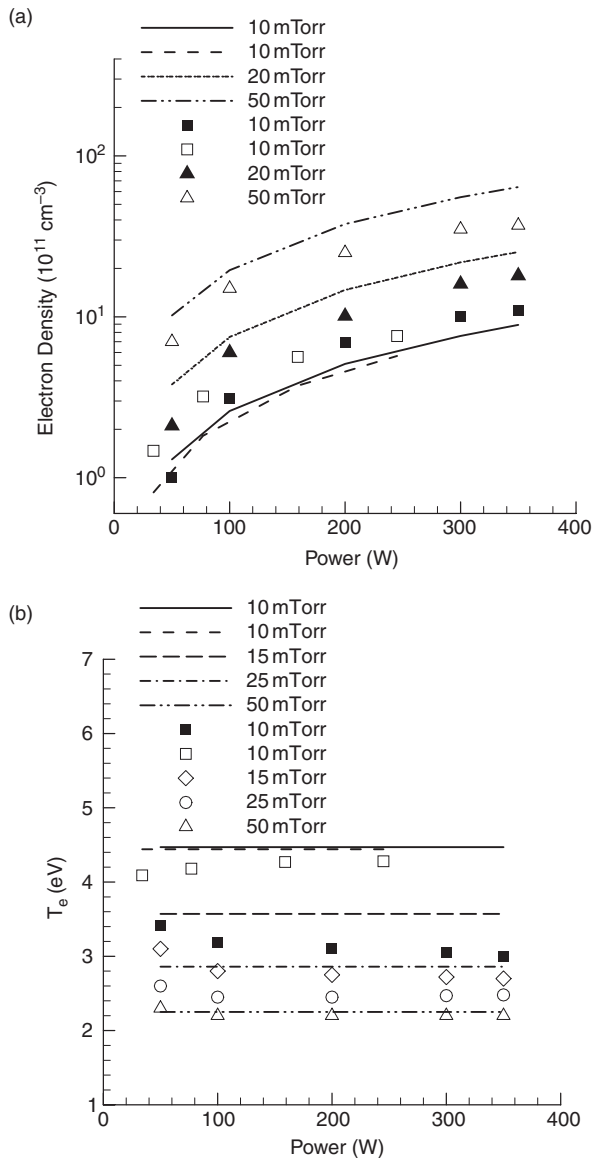
Figure 9. Comparison between simulated (lines) and experimentally measured (points) steady-state (no-pulsing) electron density ((*a*) top), and electron temperature ((*b*) bottom), as a function of power for different pressures. All data points were from [24], except for the points shown as (10 mTorr) which were obtained from [12]. Data from [24] were obtained at the reactor centre (on-axis, 19 mm from lower electrode); data from [12] were obtained on-axis, 15 mm from the lower electrode. The calculated lines correspond to the reactor centre, except for the solid line (10 mTorr) which corresponds to the location on-axis, 15 mm from the lower electrode.

Figure 10. Comparison between simulation results (lines) and experimental data (points) for steady-state (no-pulsing) electron density (top), and electron temperature (bottom), as a function of radial position for 245 W and 10 mTorr. Data were obtained from figure 11 of [12]. Axial plane for both experiment and simulation was 15 mm above the grounded (lower) electrode. The simulated values of electron density were multiplied by 1.34 to match with the experimental density at $R = 0$ (on-axis).

the low operating gas pressure (10 s of mTorr) and high plasma density. The ion density evolution during a pulse was influenced by both ambipolar diffusion and gas-phase (ionization) reactions. However, the metastable evolution was influenced mainly by gas-phase reactions, resulting in very complex spatio-temporal profiles of metastable density during a pulse. The time-average ion flux at the substrate increased almost linearly with duty ratio (at a constant peak power), but decreased with increasing pressure, in the 10–40 mTorr range investigated. The time-average ion flux to the substrate in the pulsed plasma reactor was larger than that in a CW
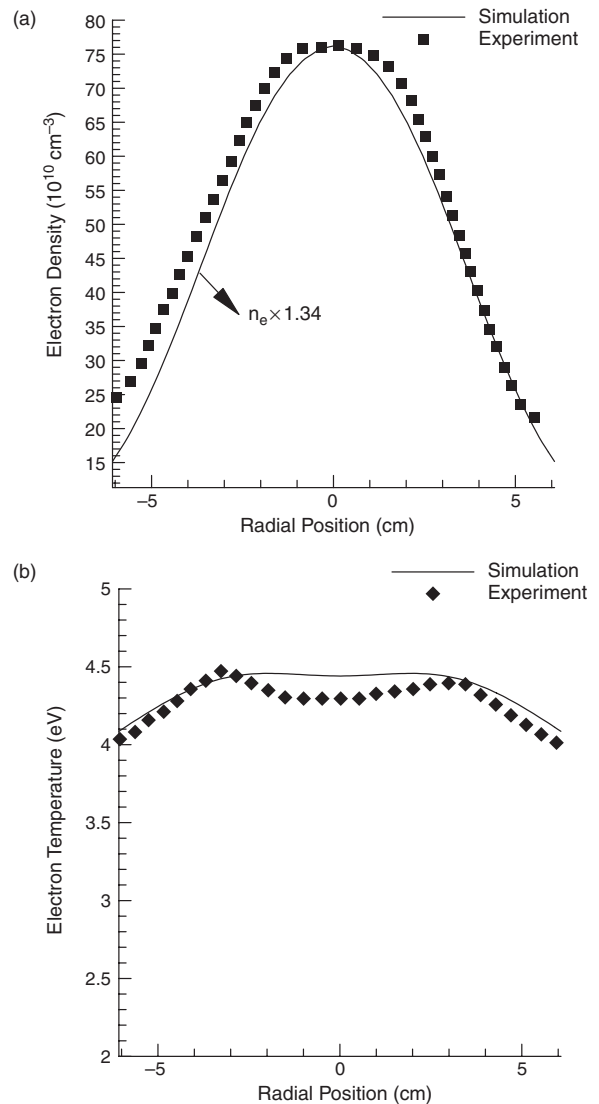
reactor, for the same energy input. The radial profile of the ion flux was very non-uniform for the GEC-ICP reactor design. Simulation results on line-integrated electron density in pulsed discharges as a function of power and pulse frequency agreed with experimental data. However, experiments showed a more complicated behaviour of electron density vs duty ratio than predicted by the simulation. Simulation results on electron density and temperature as a function of power and pressure and their spatial profiles were also in agreement with data in CW discharges.

Acknowledgments

References

[1] Lieberman M A and Lichtenberg A J 1994 *Principles of Plasma Discharges and Materials Processing* (New York: Wiley)

[2] Park S K and Economou D J 1991 *J. Electrochem. Soc.* **138** 1499
Jiang P, Economou D J and Shin C B 1995 *Plasma Chem. Plasma Process.* **15** 383
Park S-K and Economou D J 1990 *J. Electrochem. Soc.* **137** 2103

[3] Boswell R and Porteous R 1987 *J. Appl. Phys.* **62** 3123

[4] Overzet L, Verdeyen J, Roth R and Carasco F F 1987 *Mater. Res. Soc. Symp. Proc.* **98** 321
Verdeyen J, Bederman J and Overzet L 1990 *J. Vac. Sci. Technol.* A **8** 1851

[5] Sugai H, Nakamura K, Hikosaka Y and Nakamura M 1995 *J. Vac. Sci. Technol.* A **13** 887

[6] Ahn T H, Nakamura K and Sugai H 1996 *Plasma Sources Sci. Technol.* **5** 139

[7] Meyyappan M 1997 *Japan. J. Appl. Phys.* **36** (part 1) 4820

[8] Ashida S, Shin M R and Lieberman M A 1996 *J. Vac. Sci. Technol.* A **14** 391

[9] Panda S, Economou D J and Meyyappan M 2000 *J. Appl. Phys.* **87** 8323

[10] Lymberopoulos D P, Kolobov V I and Economou D J 1998 *J. Vac. Sci. Technol.* A **16** 564

[11] Midha V and Economou D J 2000 *Plasma Sources Sci. Technol.* **9** 256

[12] Miller P A, Hebner G A, Greenberg K E, Pochan P D and Aragon B P 1995 *J. Res. Natl. Inst. Stand. Technol.* **100** 427

[13] Economou D J, Feldsien J and Wise R S 1998 *Electron Kinetics and Applications of Glow Discharges (NATO Advanced Research Workshop)* ed U Kortshagen and L D Tsendin (New York: Plenum)
Wise R, Lymberopoulos D and Economou D J 1996 *Appl. Phys. Lett.* **68** 2499

[14] Lymberopoulos D P and Economou D J 1995 *J. Res. Natl. Inst. Stand. Technol.* **100** 473

[15] Nam S-K, Shin C B and Economou D J 1999 *Mater. Sci. Semicond. Process.* **2** 271

[16] Lymberopoulos D P and Economou D J 1993 *J. Appl. Phys.* **73** 3668

[17] Kolobov V I and Economou D J 1997 *Plasma Sources Sci. Technol.* **6** 1

[18] Jaeger E F, Berry L A, Tolliver J S and Batchelor D B 1995 *Phys. Plasmas* **2** 2597

[19] Midha V and Economou D J 1997 *J. Electrochem. Soc.* **144** 4062

[20] Chantry P J 1987 *J. Appl. Phys.* **62** 1141

[21] Brooks A N and Hughes T J R 1982 *Comp. Meth. Appl. Mech. Eng.* **32** 199

[22] Byrne G D and Hindmarsh A C 1987 *J. Comp. Phys.* **70** 1

[23] Hebner G A and Fleddermann C B 1997 *J. Appl. Phys.* **82** 2814

[24] Hebner G A and Miller P A 2000 *J. Appl. Phys.* **87** 8304